SUPPORTING INFORMATION

# Flexible Trilayer Cellulosic Paper Separators engineered with $BaTiO_3$ ferroelectric fillers for High Energy Density Sodium-ion Batteries

Simranjot K. Sapra,[1,2,3] Mononita Das,[4] Mir Wasim Raja,[4] Jeng-Kuei Chang,[2,3,5] and Rajendra S. Dhaka[1,*]

[1] *Department of Physics, Indian Institute of Technology Delhi, Hauz Khas, New Delhi-110016, India*
[2] *International College of Semiconductor Technology, National Yang Ming Chiao Tung University, 1001 University Road, Hsinchu 30010, Taiwan*
[3] *Department of Materials Science and Engineering, National Yang Ming Chiao Tung University, 1001 University Road, Hsinchu 30010, Taiwan*
[4] *Energy Materials and Devices Division, CSIR-Central Glass and Ceramic Research Institute, Kolkata- 700032, India*
[5] *Department of Chemical Engineering, Chung Yuan Christian University, 200 Chung Pei Road, Taoyuan, 32023 Taiwan*

(Dated: December 1, 2024)

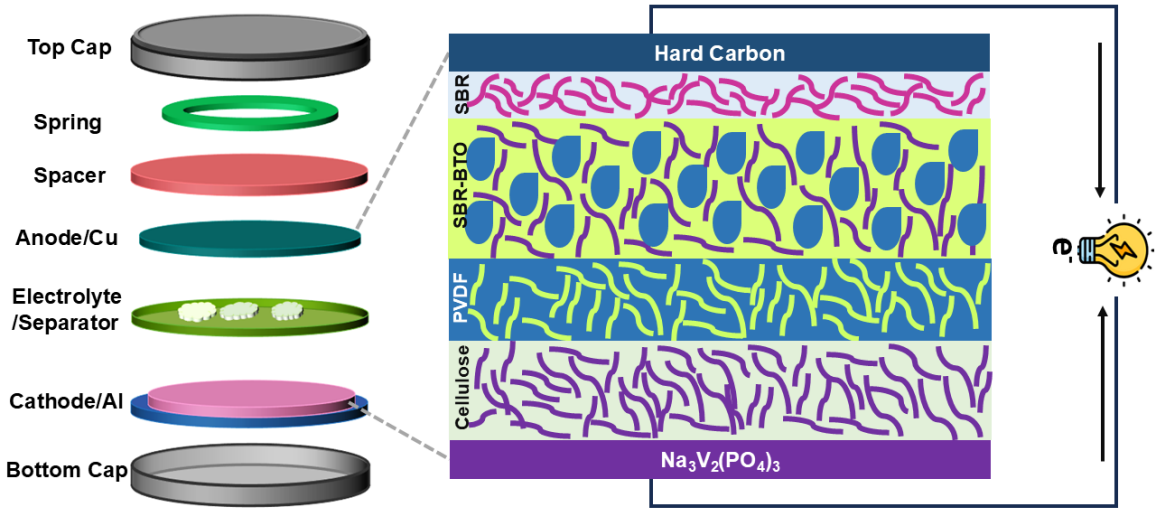


FIG. 1. Design of the full cell configuration, employing the trilayer ceramic-polymer impregnated cellulose paper separators sandwiched between the NVP and HC electrodes.

**Electrochemical performance of hard carbon in half cell configuration**: Initially, we perform the electrochemical impedance spectroscopy (EIS) measurements to understand the charge transfer resistance for the $Na^+$ ions across the electrode-electrolyte interface. The Nyquist plot for the HC anode is shown in Fig. 4(a), where the intercept of the semicircle provides the solution resistance and the diameter of the semicircle corresponds to the charge transfer resistance across the electrode/electrolyte interface. The solution and charge transfer resistors are measured as 4 Ω and 454 Ω, respectively. The galvanostatic charge-discharge (GCD) profiles in the potential window of 0.01–2.5 V at different current densities are depicted in Fig. 4(b). The GCD plot consists of two main regions: sloping and flat. The sloping region defines the storage of $Na^+$ ions in the defected carbon sites, and the flat region is indicative of intercalation of $Na^+$ ions between graphene layers and subsequent filling of nano-pores [1]. The first cycle discharge capacity at a current density of 0.05 A $g^{-1}$ is 225 mAh $g^{-1}$ with the coulombic efficiency of 96.6 %. The specific discharge capacities of 155, 105, 79, 62 and 44 mAh $g^{-1}$ are observed at the current density of 0.1, 0.2, 0.3, 0.5 and 1 A $g^{-1}$, respectively, which indicates the decreasing values with increasing current densities due to increased polarization and kinetic limitations. Interestingly, the cycle life is directly linked with the structural stability and therefore, the half cell is tested at 0.1 $Ag^{-1}$ for 110 cycles and capacity retention of 65.2% is observed with nearly 100% coulombic efficiency, exhibiting good cycling performance, as shown in Fig. 4(c). The rate performance of the HC anode at the different current densities (5 cycles each) is depicted in Fig. 4(d). It is observed that the discharge capacity decreases significantly with an increase in the current density, indicating the large impedance through SEI growth at the electrode/electrolyte interface, thereby affecting the stability.

* rsdhaka@physics.iitd.ac.in

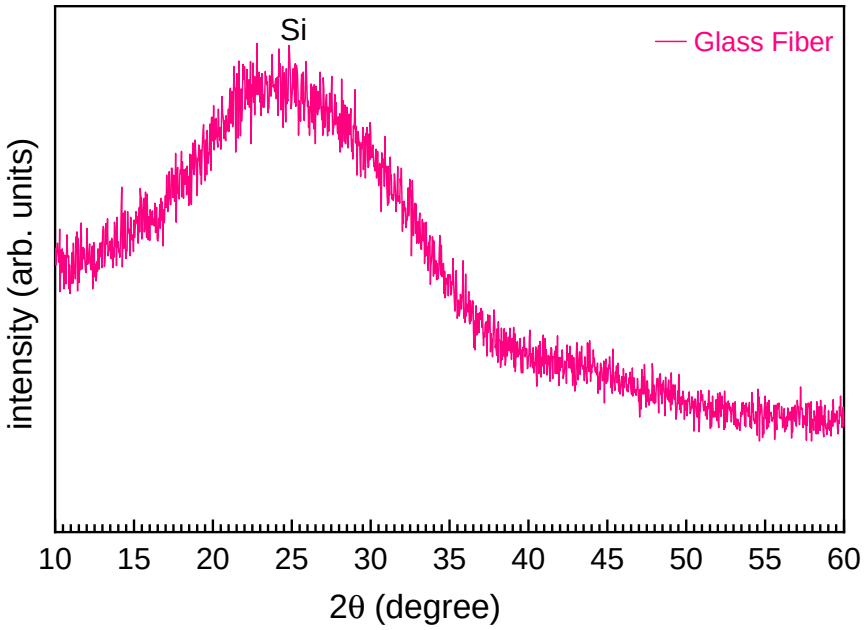


FIG. 2. The x-ray diffraction pattern of the commercial glass fiber separator (GBR-100).

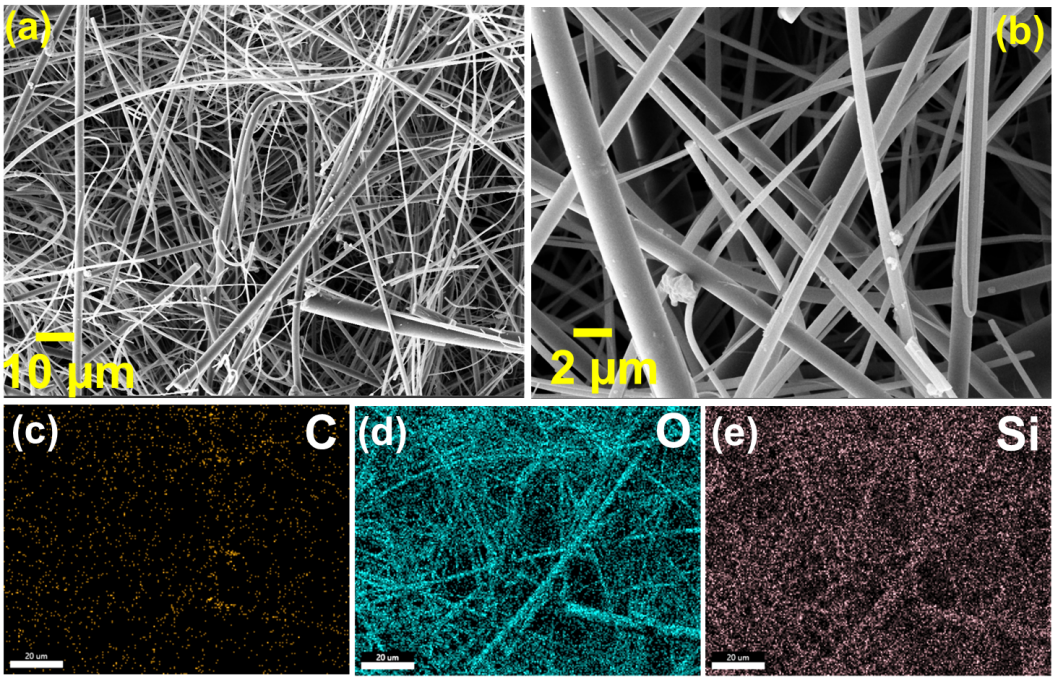


FIG. 3. The FE-SEM images of the commercial glass fiber separator with the scale of (a) 10 $\mu$m, (b) 2 $\mu$m and (c-e ) the corresponding elemental mapping over the selected region, as in (a).

To understand the sodium charge storage kinetics, we further perform cyclic voltammetry measurements in a potential window of 0.01–2.5 V. The cyclic voltammogram (CV) for the initial three cycles at 0.05 mV $s^{-1}$ are shown in Fig. 4(e). The peak at 0.5 V in the first cycle is attributed to the formation of SEI at the anodic interface. We also observe another broad peak at 0.1 V, which is related to the intercalation of sodium in the defect sites and is reflected in the sloping region of the GCD profiles, as reported in [2]. The sharp redox peaks below 0.1 V are associated with the insertion of sodium into the graphene sheets and also the adsorption of Na-ion onto the pores of HC, which correspond to the plateau region in the discharge curves. The CV curves, ranging from a scan rate of 0.05 mV $s^{-1}$ to 1 mV $s^{-1}$, are depicted in Fig. 4(f). Here, we

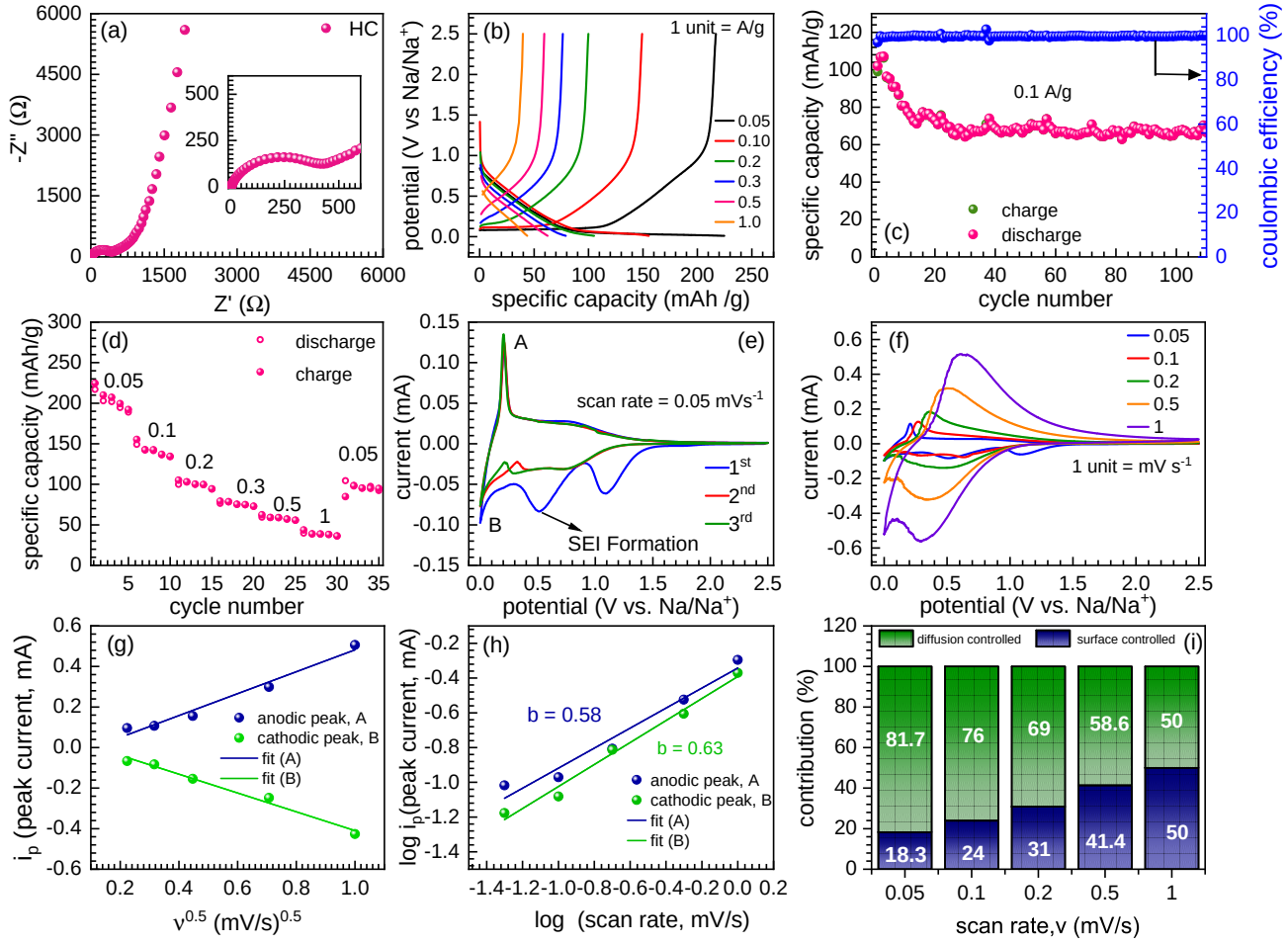


FIG. 4. The electrochemical characterisation of HC anode: (a) The Nyquist impedance spectra and the inset shows the zoomed semicircle, depicting the charge transfer resistance; (b) the galvanostatic charge-discharge profiles at various current densities; (c) the cycle life and coulombic efficiency at 0.1 A $g^{-1}$ for 110 cycles; (d) the rate performance at the different current densities (five cycles each); the CV curves for the first three cycles at the scan rate of 0.05 mV $s^{-1}$ (e) and (f) different current densities (0.05–1 mV $s^{-1}$); (g) the peak current vs. scan rate; (h) log of the peak current vs. log of scan rates; (i) the contribution of the capacitive and diffusive components from the total current at all scan rates.

find that the displacement of oxidation peaks towards the higher potential and reduction peaks towards the lower potential with the increasing scan rates, which is associated with an increase in polarization due to increased current density, similar to GCD profiles. Concurrently, the magnitudes of oxidation and reduction peaks also amplify as the scan rates rise, arising from the existence of electric double-layer capacitors and capacitor current is in linear relationship with the scan rate [3]. The peak currents for the HC anode at all the scan rates are calculated, and their linear relationship is shown in Fig. 4(g), respectively. Assuming that current obeys the power law relation, $i = a\nu^b$; where $a$ and $b$ are constants, $i$ and $\nu$ are the peak current and scan rate. The constant, $b$ is an indicator of the type of Na ion (de)intercalation process involved in the charge storage and the value of $b$ is calculated from the slope of the $\log(i_p)$ and $\log(\nu)$ plot, as shown in Fig. 4(h). As reported in the literature, if the value of $b = 0.5$, the charge storage mechanism is termed diffusion-controlled (faradaic), and the value of $b = 1.0$ defines the charge storage mechanism as the surface-controlled (capacitive) and if the value lies between 0.5 and 1, charge storage mechanism is considered as a combination of the both the above, termed as pseudo-capacitive [5]. Herein, the values of $b$ are calculated to be 0.58 and 0.63 for the anodic and cathodic peaks of HC anode, respectively, signifying the involvement of both the bulk (phase change) and surface (adsorption on the surface) intercalation of Na ions. The contributions are quantified by the sum of capacitive ($k_1\nu$) and diffusion-controlled ($k_2\nu^{1/2}$) through the equation $i(V) = k_1\nu + k_2\nu^{1/2}$ and values are depicted in Fig. 4(i) [6]. The detailed electrochemical performance of the NVP half cells is shown in our work [4].

The pore size distributions of paper separators with different polymer concentration in lamination layer are presented in Fig. 5. Their surface area, average pore diameter and total pore volume are also shown in Table 1 in the main text file. The Barrett-Joyner-Halenda (BJH) plots of separator samples reveal the average pore radius of the developed paper separators is mostly mesoporous in nature with their average pore diameters lying in the range of 3–4 nm. The actual pore sizes of

the separators should be much larger (in micrometre region) since paper is made up of cross-linking cellulose fibers creating random pore spaces among them. Although, the BJH is not a suitable method to determine pore size of such membranes, it has been incorporated to provide an overview of the pore characteristics of the developed paper separators.

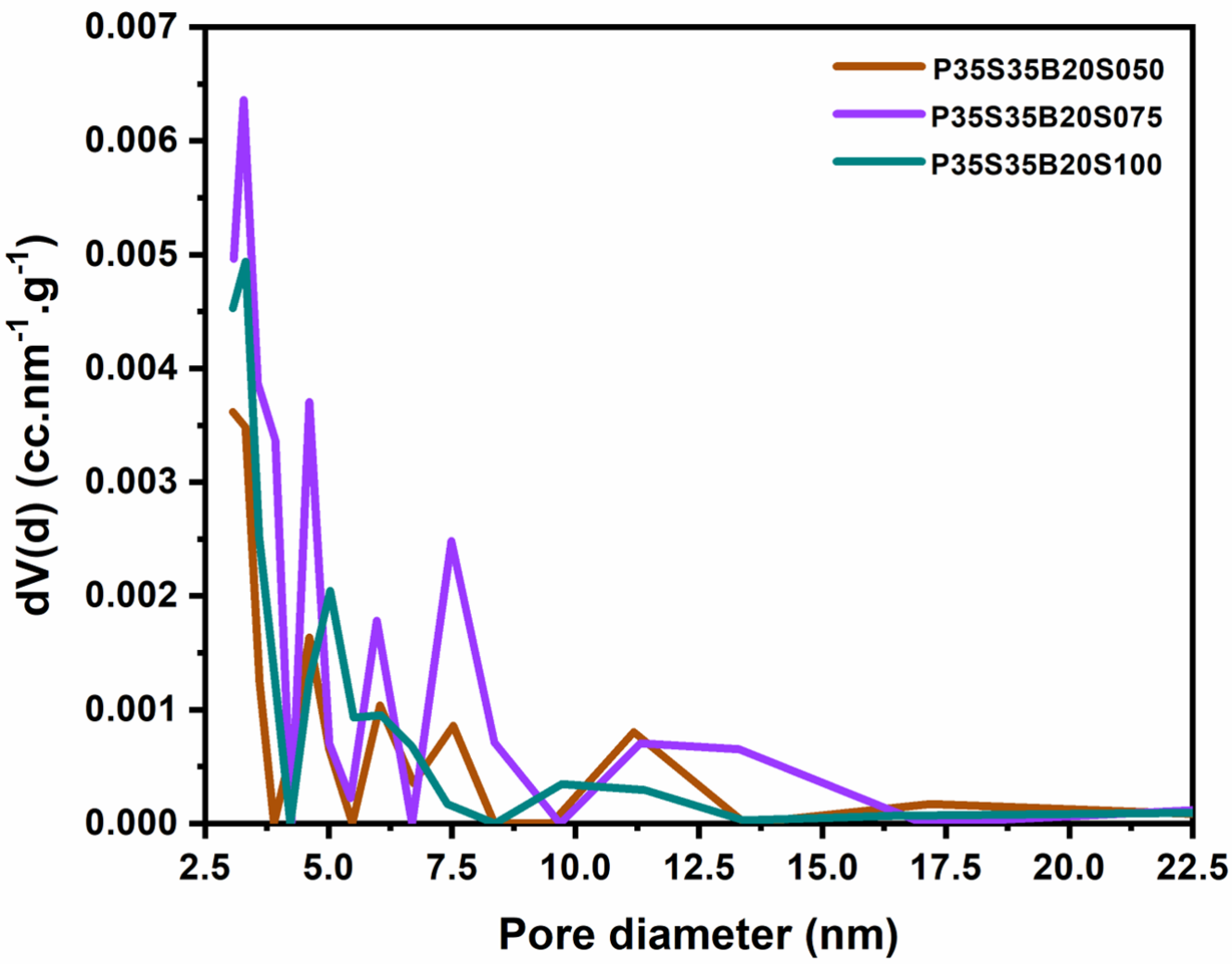


FIG. 5. The Barrett-Joyner-Halenda (BJH) plots of the developed paper separators.

To evaluate the tensile strength of the separators, stress vs strain curves are presented for both machine direction (MD) and transverse direction (TD) in Fig. 6(b). The values of the tensile stress (MPa) and tensile strain (%) along the MD and TD directions for all paper separators are summarised in Table. S1. Furthermore, a qualitative view of thermal shrinkage properties at temperature of 200°C for developed paper separators is presented in Fig. 7. It is observed that the developed paper separators retain their structural integrity at high temperatures, even at 200°C. This demonstrates higher dimensional stability of the developed paper separators at elevated temperatures, ensuring their safe use inside sodium-ion cells.

TABLE S1. The summary of the tensile properties of the developed paper separators.

| separator code | tensile stress (MPa) | | tensile strain (%) | | Young modulus (MPa) | |
|---|---|---|---|---|---|---|
| | MD | TD | MD | TD | MD | TD |
| P35S35B20S050 | 49.32 | 25.08 | 4.47 | 6.56 | 2897.48 | 1057.02 |
| P35S35B20S075 | 48.78 | 27.57 | 5.80 | 9.61 | 1926.71 | 745.37 |
| P35S35B20S100 | 46.61 | 25.08 | 4.26 | 7.78 | 2938.61 | 937.25 |

The FE-SEM and elemental mappings of the folded S075 separator are shown in the Fig. 8. We observe that there is

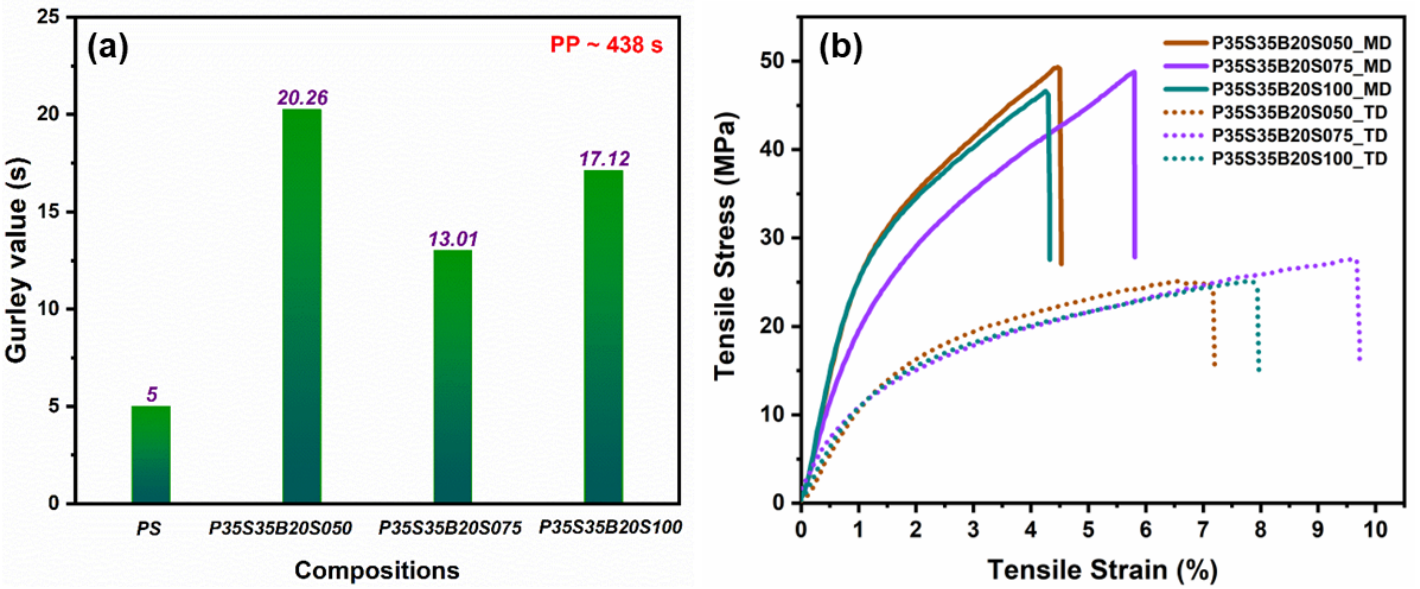


FIG. 6. (a) The variation of Gurley values of untreated paper substrate (PS) and the developed separators (P35S35B20S050, P35S35B20S075 and P35S35B20S100), (b) The stress versus strain plots of the developed paper separators in machine direction (MD) as well as in transverse direction (TD).

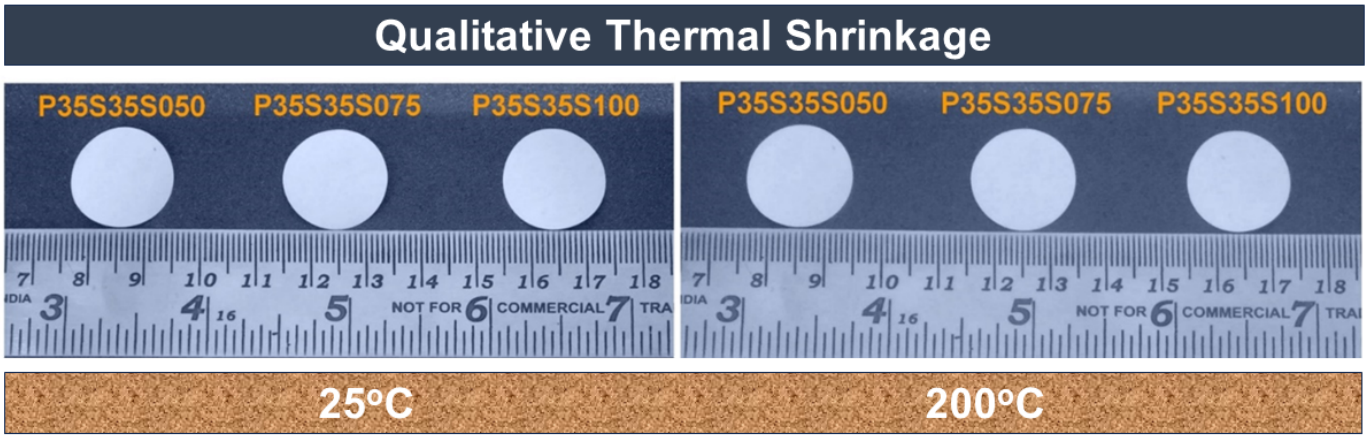


FIG. 7. The qualitative thermal shrinkage measurement of the developed paper separators at 25°C and 200°C.

no significant change in the distribution of the elements of the paper membrane upon undergoing folding, which shows the mechanical stability and flexibility of these paper membranes.

To further probe the sodium charge storage kinetics in full cells, we perform the cyclic voltammetry (CV) measurements at different scan rates of 0.05–1.0 mV/s in a potential window of 2.0–4.3 V. The cyclic voltammogram of the paper separator S075 in the full cell configuration are shown in Fig. 9(a). At the lower scan rate of 0.05 $mVs^{-1}$, the oxidation current at 3.42 V corresponds to the extraction of Na ions from the Na2 site and the reduction current starting at 3.13 V reflects the insertion of Na ions at the Na2 site [7]. The presence of redox peaks at a lower scan rate in the CV profile shows the diffusion-controlled (faradaic) behavior, corresponding to the intercalation of Na ions in the bulk material, which is well in agreement with the NVP half-cell profile [4]. Furthermore, we observe the shift in oxidation peaks towards the higher potential and reduction peaks towards the lower potential with increasing the scan rate, as shown in Fig. 9(a) for the full cell with NVP cathode and HC anode, which are associated with increased polarization at higher current density. Concurrently, the magnitude of oxidation and reduction peaks also amplify as the scan rates rise, arising from the existence of electric double-layer capacitors, and the capacitive current follows the linear relationship with the scan rate [8]. However, it is found that capacitive contribution increases with the scan rates (the capacitive current is directly proportional to the $\nu$, as explained in the above section for hard carbon) with the broadening of peak profiles, confirming that charge storage occurs through surface-controlled capacitive behavior [5, 10]. As the sodium inventory becomes limited in the full cells, which comes from

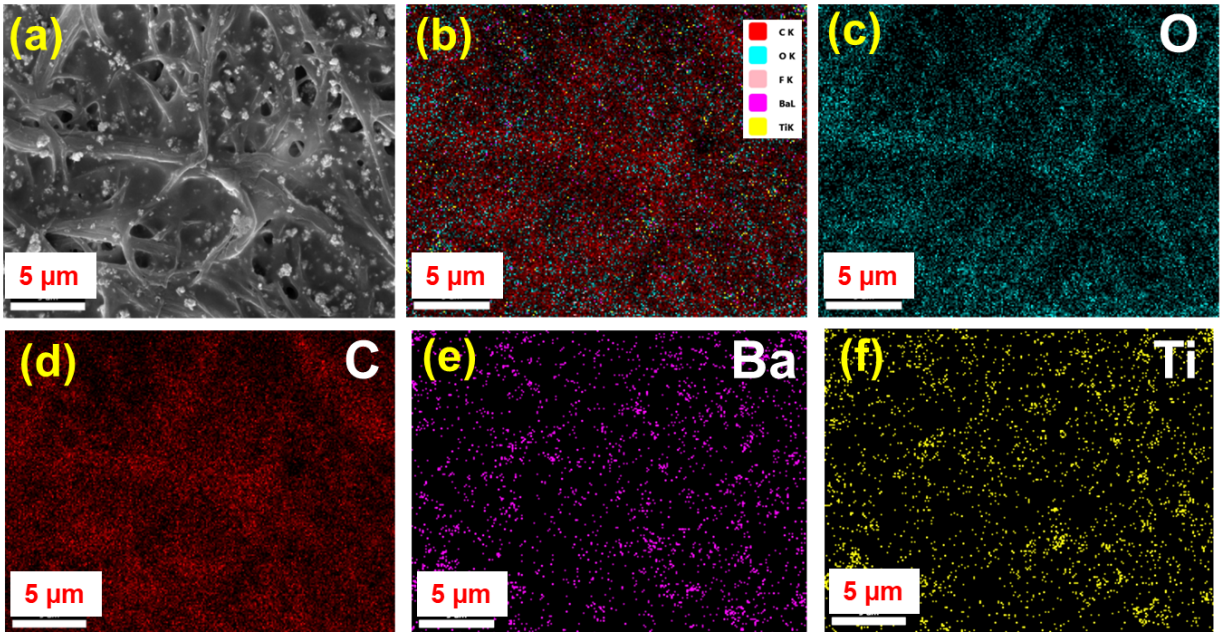


FIG. 8. (a) The FE-SEM image of the folded region of the S075 separator, and (b–f) the corresponding elemental mappings (O, C, Ba, Ti) for the selected region of the folded part.

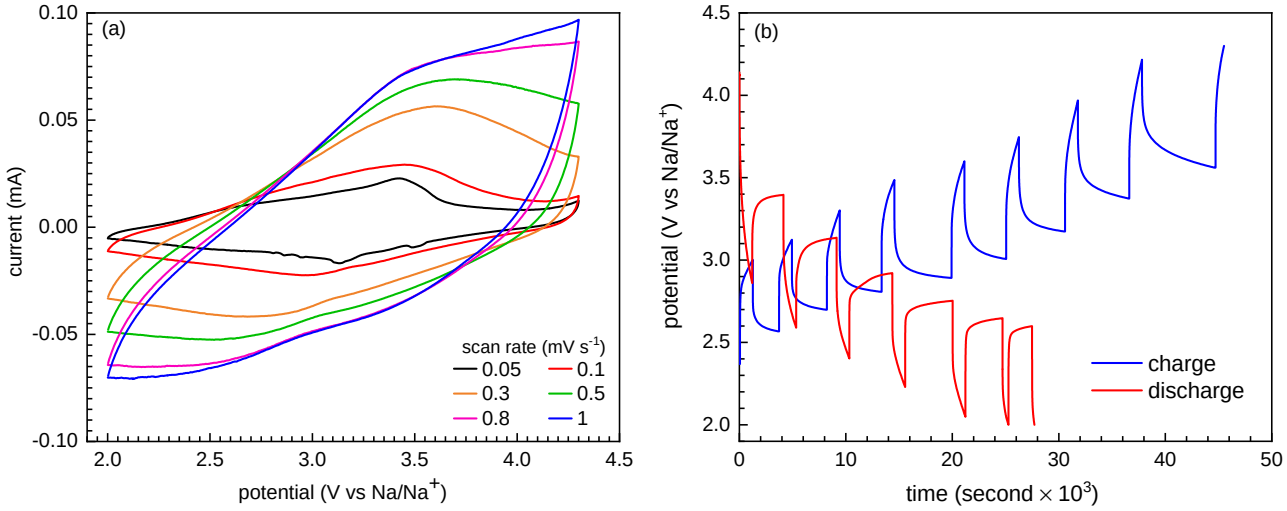


FIG. 9. (a) The CV curves at the different scan rates (0.05–1.0 mV $s^{-1}$) and (b) the GITT measurements at a current rate of 0.3 C in the potential window of 2.0–4.3V for the NVP cathode using the S075 separator with HC anode in the full cell configuration.

the NVP cathode, it causes fading in the charge storage through the reconstruction of SEI, and the sodium ions are adsorbed on the capacitive double-layer at the electrode/electrolyte interface due to limited diffusion time with the rise of scan rate [9]. In addition, we perform the galvanostatic intermittent titration technique (GITT) measurements for the S075 separator at a current rate of 0.3 C in the potential window of 2.0–4.3V. Here, measurement is performed using the pulse time of 30 mins, followed by a relaxation period of 3 hrs for the better homogenization of the sodium ions and allow the system to reach quasi-equilibrium. The GITT profiles during the charge and discharge for the full cell are represented in Fig. 9(b).

[1] X. Dou, I. Hasa, D. Saurel, C. Vaalma, L. Wu, D. Buchholz, D. Bresser, S. Komaba and S. Passerini, Hard carbons for sodium-ion batteries: Structure, analysis, sustainability, and electrochemistry. Materials Today, **23**, 87 (2019).
[2] C. Bommier, T. W. Surta, M. Dolgos and X. Ji, New mechanistic insights on Na-ion storage in nongraphitizable carbon, Nano

Letters, **15**, 5888 (2015).
[3] C. Liu, X. Jiang, Q. Huang, Y. Chen and L. Guo, Simultaneous defect regulation by p–n type co-substitution in a $Na_3V_2(PO_4)_3$/C cathode for high-performance sodium ion batteries, Dalton Transactions **51**, 10943 (2022).
[4] S. K. Sapra, J.-K. Chang and R. S. Dhaka. Improved electrochemical performance of NASICON type $Na_3V_{2-x}Co_x(PO_4)_3$/C ($x$ =0–0.15) cathode for high rate and stable sodium-ion batteries. ACS Appl. Mater. Interfaces, **16**, 43535–43547 (2024).
[5] T. S. Mathis, N. Kurra, X. Wang, D. Pinto, P. Simon, and Y. Gogotsi. Energy storage data reporting in perspective—guidelines for interpreting the performance of electrochemical energy storage systems, Adv. Energy Mater. **9**, 1902007 (2019).
[6] X. Pu, D. Zhao, C. Fu, Z. Chen, S. Cao, C. Wang and Y. Cao, Understanding and calibration of charge storage mechanism in cyclic voltammetry curves, Angew. Chem. **60**, 21310–21318 (2021).
[7] Q. Zheng, H. Yi, X. Li and H. Zhang, Progress and prospect for NASICON-type $Na_3V_2(PO_4)_3$ for electrochemical energy storage. Journal of Energy Chemistry, **27**, 1597–1617 (2018).
[8] J. Pati and R. S. Dhaka, Mixed Polyanionic $NaFe_{1.6}V_{0.4}(PO_4)(SO_4)_2$@CNT Cathode for Sodium-ion Batteries: Electrochemical Diffusion Kinetics and Distribution of Relaxation Time Analysis at Different Temperatures. J. Power Sources, **609**, 234646 (2024).
[9] X. Yang, Z. Zuo, H. Wang, Q. Chen, H. Zhang, Z. Huang, B. Wu and H. Zhou, The contradiction between the half-cell and full-battery evaluations on the tungsten-coating $LiNi_{0.5}Co_{0.2}Mn_{0.3}O_2$ cathode, Electrochim. Acta, **180**, 604–609 (2015).
[10] Y. Gogotsi and R. M. Penner, Energy storage in nanomaterials–capacitive, pseudocapacitive, or battery-like? ACS Nano, **12**, 2081–2083 (2018).